



# ALMA Survey of Orion Planck Galactic Cold Clumps (ALMASOP): Detection of a Dense SiO Jet in the Evolved Protostellar Phase

Somnath Dutta<sup>1</sup>, Chin-Fei Lee<sup>1</sup>, Doug Johnstone<sup>2,3</sup>, Tie Liu<sup>4</sup>, Naomi Hirano<sup>1</sup>, Sheng-Yuan Liu<sup>1</sup>, Jeong-Eun Lee<sup>5</sup>, Hsien Shang<sup>1</sup>, Ken'ichi Tatematsu<sup>6,7</sup>, Kee-Tae Kim<sup>8,9</sup>, Dipen Sahu<sup>1</sup>, Patricio Sanhueza<sup>7,10</sup>, James Di Francesco<sup>2</sup>, Kai-Syun Jhan<sup>1</sup>, Chang Won Lee<sup>8,9</sup>, Woojin Kwon<sup>11,12</sup>, Shanghuo Li<sup>8</sup>, Leonardo Bronfman<sup>13</sup>, Hong-li Liu<sup>14</sup>, Alessio Traficante<sup>15</sup>, Yi-Jehng Kuan<sup>1,16</sup>, Shih-Ying Hsu<sup>1</sup>, Anthony Moraghan<sup>1</sup>, Chun-Fan Liu<sup>1</sup>, David Eden<sup>17</sup>, Archana Soam<sup>18</sup>, and Qiuyi Luo<sup>4</sup>  
(ALMASOP Team)

<sup>1</sup> Institute of Astronomy and Astrophysics, Academia Sinica, Roosevelt Road, Taipei 10617, Taiwan, R.O.C.; [sdutta@asiaa.sinica.edu.tw](mailto:sdutta@asiaa.sinica.edu.tw), [cflee@asiaa.sinica.edu.tw](mailto:cflee@asiaa.sinica.edu.tw)

<sup>2</sup> National Research Council of Canada, Herzberg, Astronomy and Astrophysics Research Centre, 5071 West Saanich Road, V9E 2E7 Victoria (BC), Canada

<sup>3</sup> Department of Physics and Astronomy, University of Victoria, Victoria, BC V8P 5C2, Canada

<sup>4</sup> Shanghai Astronomical Observatory, Chinese Academy of Sciences, 80 Nandan Road, Shanghai 200030, People's Republic of China

<sup>5</sup> School of Space Research, Kyung Hee University, Yongin-Si, Gyeonggi-Do 17104, Republic of Korea

<sup>6</sup> Nobeyama Radio Observatory, National Astronomical Observatory of Japan, National Institutes of Natural Sciences, 462-2 Nobeyama, Minamimaki, Minamisaku, Nagano 384-1305, Japan

<sup>7</sup> Department of Astronomical Science, SOKENDAI (The Graduate University for Advanced Studies), 2-21-1 Osawa, Mitaka, Tokyo 181-8588, Japan

<sup>8</sup> Korea Astronomy and Space Science Institute (KASI), 776 Daedeokdae-ro, Yuseong-gu, Daejeon 34055, Republic of Korea

<sup>9</sup> University of Science and Technology, Korea (UST), 217 Gajeong-ro, Yuseong-gu, Daejeon 34113, Republic of Korea

<sup>10</sup> National Astronomical Observatory of Japan, National Institutes of Natural Sciences, 2-21-1 Osawa, Mitaka, Tokyo 181-8588, Japan

<sup>11</sup> Department of Earth Science Education, Seoul National University, 1 Gwanak-ro, Gwanak-gu, Seoul 08826, Republic of Korea

<sup>12</sup> SNU Astronomy Research Center, Seoul National University, 1 Gwanak-ro, Gwanak-gu, Seoul 08826, Republic of Korea

<sup>13</sup> Departamento de Astronomía, Universidad de Chile, Casilla 36-D, Santiago, Chile

<sup>14</sup> Department of Astronomy, Yunnan University, Kunming 650091, People's Republic of China

<sup>15</sup> IAPS-INAF, via Fosso del Cavaliere 100, I-00133, Rome, Italy

<sup>16</sup> Department of Earth Sciences, National Taiwan Normal University, Taipei, Taiwan, R.O.C.

<sup>17</sup> Astrophysics Research Institute, Liverpool John Moores University, IC2, Liverpool Science Park, 146 Brownlow Hill, Liverpool, L3 5RF, UK

<sup>18</sup> SOFIA Science Center, Universities Space Research Association, NASA Ames Research Center, Moffett Field, CA 94035, USA

Received 2021 June 22; revised 2021 October 26; accepted 2021 October 26; published 2022 January 20

## Abstract

Jets and outflows trace the accretion history of protostars. High-velocity molecular jets have been observed from several protostars in the early Class 0 phase of star formation, detected with the high-density tracer SiO. Until now, no clear jet has been detected with SiO emission from isolated evolved Class I protostellar systems. We report a prominent dense SiO jet from a Class I source G205S3 (HOPS-315:  $T_{\text{bol}} \sim 180$  K, spectral index  $\sim 0.417$ ), with a moderately high mass-loss rate ( $\sim 0.59 \times 10^{-6} M_{\odot} \text{ yr}^{-1}$ ) estimated from CO emission. Together, these features suggest that G205S3 is still in a high-accretion phase, similar to that expected of Class 0 objects. We compare G205S3 to a representative Class 0 system G206W2 (HOPS-399) and literature Class 0/I sources to explore the possible explanations behind the SiO emission seen at the later phase. We estimate a high inclination angle ( $\sim 40^{\circ}$ ) for G205S3 from CO emission, which may expose the infrared emission from the central core and mislead the spectral classification. However, the compact 1.3 mm continuum,  $\text{C}^{18}\text{O}$  emission, location in the bolometric luminosity to submillimeter fluxes diagram, outflow force ( $\sim 3.26 \times 10^{-5} M_{\odot} \text{ km s}^{-1} \text{ yr}^{-1}$ ) are also analogous to that of Class I systems. We thus consider G205S3 to be at the very early phase of Class I, and in the late phase of *high accretion*. The episodic ejection could be due to the presence of an unknown binary, a planetary companion, or dense clumps, where the required mass for such high accretion could be supplied by a massive circumbinary disk.


*Unified Astronomy Thesaurus concepts:* [Low mass stars \(2050\)](#); [Stellar jets \(1607\)](#); [Stellar winds \(1636\)](#); [Protostars \(1302\)](#); [Astrochemistry \(75\)](#); [Star formation \(1569\)](#); [Stellar mass loss \(1613\)](#); [Young stellar objects \(1834\)](#); [Stellar evolution \(1599\)](#)

## 1. Introduction

During the earliest phases of star formation, jets and outflows play a crucial role in mediating protostellar accretion. Previous observations suggest that jets can efficiently remove the excess angular momentum from the surfaces of circumstellar disks and allow material to fall onto the central sources (see reviews by

Bally 2016; Lee 2020, and references therein). Therefore, jets may delineate the accretion history of protostars. Despite this important role, the jet launching timescale over protostellar evolution is not yet well constrained.

The protostellar spectral classes, 0 and I, are observationally defined and not clearly distinct in terms of evolution. Protostars with bolometric temperature  $T_{\text{bol}} > 70$  K are classified as Class I (Chen et al. 1995), and typically have spectral indexes,  $\alpha_{\text{IR}} > 0.3$  (Furlan et al. 2016). The Class 0 sources are embedded within dense envelopes and have sufficient surrounding material to exhibit typically very high-accretion rates onto the protostar.

 Original content from this work may be used under the terms of the [Creative Commons Attribution 4.0 licence](#). Any further distribution of this work must maintain attribution to the author(s) and the title of the work, journal citation and DOI.

During this phase, protostars usually show outflows with very high mass-loss rates  $\sim 10^{-6}$ – $10^{-7} M_{\odot} \text{ yr}^{-1}$ , which could produce high-density jets ( $(5\text{--}10) \times 10^6 \text{ cm}^{-3}$ ) (Ellerbroek et al. 2013; Lee 2020). Due to its high critical density, the SiO (5–4) molecular transition is the most commonly observed tracer of such high-density material (Gibb et al. 2004; Podio et al. 2015, 2021). With time, the envelope material reduces and the protostar moves from Class 0 through Class I, and on to the Class II phase. Both the accretion and mass-loss rates typically decrease with protostellar evolution. Therefore, SiO emission in jets is usually seen in the Class 0 sources. Faint SiO emission is also detected along the jet axis of a few transition Class 0-to-Class I sources (Podio et al. 2021). A Class I protostellar system, SVS13A was found with SiO knots in previous observations (Bachiller et al. 2000; Lefèvre et al. 2017). However, SVS13A is located in a multiple system HH 7/11 with a few outflow/jets in the region, and is a binary protostellar system composed of VLA4A and VLA4B, where VLA4B is identified as the base of the jet (Lefèvre et al. 2017). The spectral classification of the components of such a binary/multiple based on infrared observations could be largely affected by the multiplicity. No clear jets with SiO emission have been previously observed in an isolated source in the evolved Class I phase.

The gas content of the jets transitions from being predominantly molecular to mostly atomic, during evolution from Class 0 to Class II. The jets in the younger sources, such as those in the Class 0 phase, are predominantly detected via molecular gas tracers, e.g., CO, SiO, and SO in the (sub) millimeter and  $\text{H}_2$  at infrared wavelengths. Conversely, in the older Class I and II populations, the jets are mainly traced by the atomic and ionized gas, e.g., O,  $\text{H}\alpha$ , and  $\text{S II}$  (Bally 2016; Lee 2020).

In this paper, we report the surprising detection of a Class I source with a clear protostellar jet seen in SiO by the Atacama Large Millimeter/submillimeter Array (ALMA). The system G205.46-14.56S3 (hereafter, G205S3) has  $T_{\text{bol}} = 180 \pm 33 \text{ K}$  and  $L_{\text{bol}} = 6.4 \pm 2.4 L_{\odot}$  (HOPS-315; Furlan et al. 2016; Dutta et al. 2020). We compare this system with ALMA observations of a representative Class 0 protostar, G206.93-16.61W2 (hereafter, G206W2), with  $T_{\text{bol}} = 31 \pm 10 \text{ K}$  and  $L_{\text{bol}} = 6.3 \pm 3.0 L_{\odot}$  (HOPS-399; Furlan et al. 2016; Dutta et al. 2020). Both sources exhibit very high mass-loss rates; however, the SiO jets present very different inclination angles. We first quantify the outflow characteristics and then discuss the evolutionary state of these two systems in terms of their observed sky orientation.

## 2. Observations

The ALMA observations of G205S2 and G206W2 were performed as part of the ALMA Survey of Orion Planck Galactic Cold Clumps (ALMASOP) project (Project ID: 2018.1.00302.S; PI: T. Liu) in Band 6 during Cycle 6, from 2018 October to 2019 January, toward 72 fields (see Dutta et al. 2020 for more details on the ALMASOP). This paper utilizes the low-/high-velocity outflow tracer CO  $J=2-1$  (230.53800 GHz), the high-velocity jet tracer SiO  $J=5-4$  (217.10498 GHz), the envelope tracer  $\text{C}^{18}\text{O}$   $J=2-1$  (219.56035 GHz), and 1.3 mm dust continuum emission. The acquired visibility data were calibrated using the standard pipeline in CASA 5.4 (McMullin et al. 2007). The CO  $J=2-1$ , SiO  $J=5-4$ , and  $\text{C}^{18}\text{O}$   $J=2-1$  emission maps were created with the TCLEAN task using a robust weighting factor of +0.5 on a combination of three visibility data sets (i.e., TM1

+TM2+ACA) providing typical synthesized beam sizes of  $\sim 0''.37 \times 0''.32$ ,  $\sim 0''.41 \times 0''.34$ , and  $\sim 0''.39 \times 0''.32$ , respectively. The velocity resolution is  $1.4 \text{ km s}^{-1}$ . The continuum maps were created using TCLEAN and a+0.5 robust weighting down to a threshold of  $3\sigma$  theoretical sensitivity with the synthesized beam size of  $\sim 0''.38 \times 0''.34$ . More details on these observations and analyses are presented in Dutta et al. (2020).

## 3. Results

### 3.1. Detection of Molecular Jet in SiO Emission

Figures 1(a) and (c) display ALMA maps of the two jets in SiO (5–4) at  $\sim 140 \text{ au}$  resolution along with the high-velocity CO outflow contours overplotted in blue and red.

Figures 1(b) and (d) show the position–velocity (PV) diagrams of the SiO emission traced along each jet-axis direction. The systemic velocities are obtained from peak  $\text{C}^{18}\text{O}$  emission and are marked in Figures 1(b) and (d) (Column 3 of Table 1). G205S3 and G206W2 exhibit line-of-sight projected maximum velocities of  $V_{\text{max, SiO}} \sim 120$  and  $106 \text{ km s}^{-1}$ , respectively (Column 5 of Table 1).

The jet from G205S3 is highly collimated, whereas that from G206W2 is relatively extended spatially. Both jets exhibit knots (marked as B1, B2, ... in the blue lobe and R1, R2.... in red lobe), which are possibly formed by a chain of internal shocks via a semi-periodic variation in the jet velocity (Moraghan et al. 2016; Wang et al. 2019). We estimate mean line-of-sight jet velocities from the peak positions of the knot structures, yielding  $V_{j, \text{obs}} \sim 80$  and  $50 \text{ km s}^{-1}$  for G205S3 and G206W2, respectively. Considering projection effects due to the inclination angle ( $i$ ), the corrected velocities ( $V_{j, \text{corr}}$ ) are related as  $V_{j, \text{obs}} = V_{j, \text{corr}} \sin(i)$ . We evaluate the mean plane-of-sky separations for consecutive knots of  $\Delta r_{\text{obs}} = 2''.7$  and  $2''.5$  for G205S3 and G206W2, respectively. These measurements can be expressed as the corrected distances ( $\Delta r_{\text{corr}}$ ) using the projection angles,  $\Delta r_{\text{obs}} = \Delta r_{\text{corr}} \cos(i)$ .

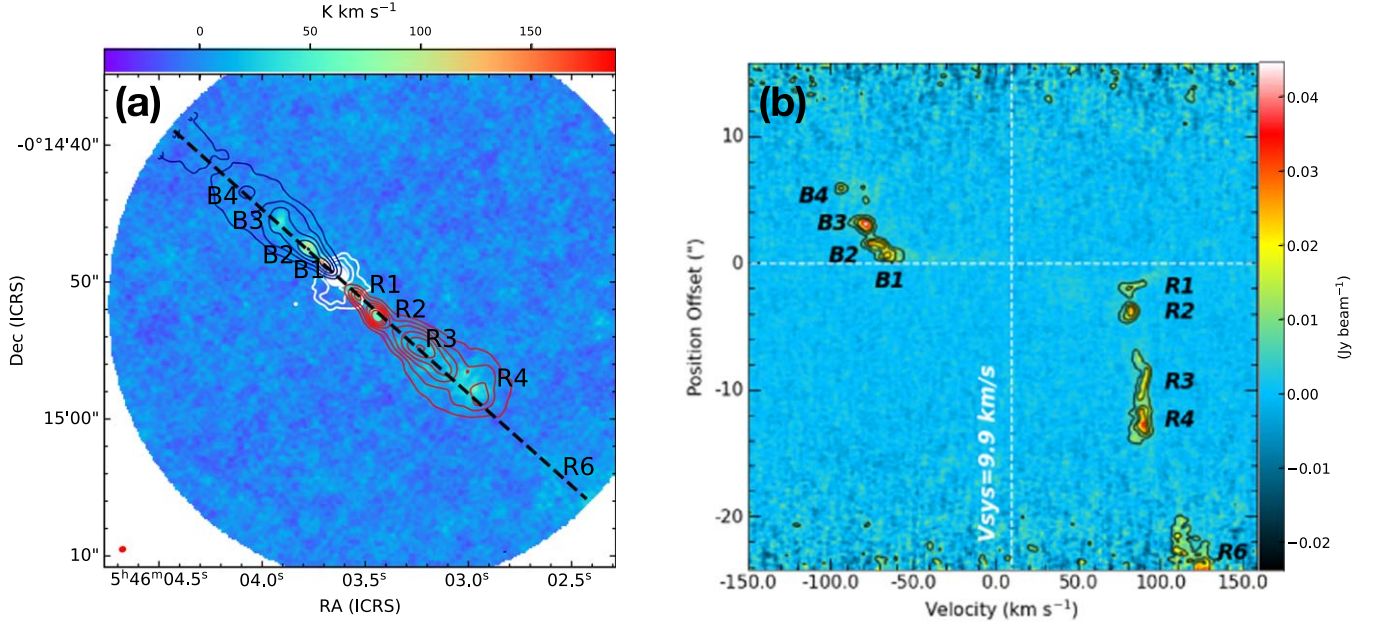
### 3.2. Outflow Shell in CO: Inclination Angle

Following the simple analytical model by Lee et al. (2000), we determine the physical structure of the outflow using the CO emission. In this model, the molecular outflow can be represented as a radially expanding parabolic shell driven by the underlying wide-angle wind. In a cylindrical coordinate system, the outflow shell can be described by the equation  $z = CR^2$ , where  $z$  is the outflow axis and  $R$  is the radial distance from that axis (for a schematic diagram, see Figure 21 by Lee et al. 2000).

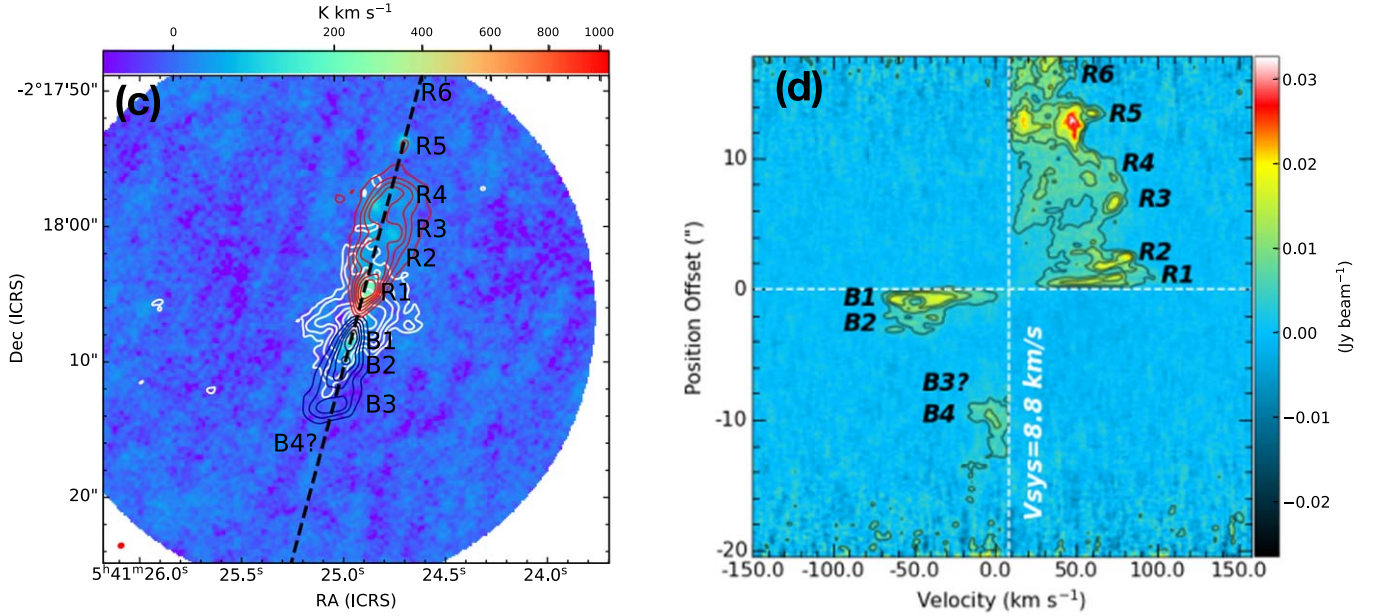
Figure 2(a) displays the CO outflow components of G205S3. We fitted a parabola to the outermost contour closer to the real outflow cavity wall, yielding  $C = 0.20$  and  $0.26$  for the blue and red lobe, respectively. Using these  $C$  values, we then fitted parabolas for the low-velocity outflow cavities in the PV diagram (Figure 2(b)) for the corresponding outflow lobes, which provided best fits of inclination angle,  $i = 40^\circ \pm 8^\circ$  for both the lobes. Notice that the apparent continuum center for this object is shifted in position from the center of the *neck* toward the blue lobe due to the projection effect (Figure 2(a)). Similarly, we estimated  $C$  values of  $0.90$  and  $0.80$  (Figure 2(c)) for the blue and red lobes of G206W2, respectively. The best fitted parabolas in the PV diagram for G206W2 provide an inclination of  $i = 10^\circ \pm 5^\circ$  for both lobes (Figure 2(d)). Here,



## G205.46-14.56S3



## G206.93-16.61W2



**Figure 1.** (a) ALMA SiO  $J = 5-4$  maps of G205S3 jet at spatial resolution of 140 au with sensitivity of  $\sim 9.5$  K. High-velocity  $^{12}\text{CO}(2-1)$  contours are overlaid for blueshifted (blue) and redshifted (red) lobes at  $3 \times (1, 2, 3, 6, 9)\sigma$ , where  $\sigma = 51$  mJy beam $^{-1}$ . The continuum contours (white) are at  $\sum_{n=0,1,2,3,\dots} 3 \times 2^n \sigma$ , where  $\sigma = 80$   $\mu\text{Jy beam}^{-1}$ . The beam size of  $\sim 0''.41 \times 0''.34$  for SiO emission is shown in red on lower left. The black dashed line indicates the jet axis. (b) PV diagrams across the jet axis. The vertical dashed lines indicate the systemic velocity. The contour levels start from  $3\sigma$  with steps of  $3\sigma$ , where  $\sigma = 2$  mJy beam $^{-1}$ . The location of knots is marked in the blue lobe (B1, B2, ...) and red lobe (R1, R2, ...). (c) ALMA SiO  $J = 5-4$  maps of G2056W2 with sensitivity of  $\sim 12$  K. All the symbols are the same as panel (a). The higher velocity  $^{12}\text{CO}(2-1)$  have sensitivity  $\sigma = 53$  mJy beam $^{-1}$ . The continuum emission have sensitivity  $\sigma = 150$   $\mu\text{Jy beam}^{-1}$ . (d) PV diagram across the jet axis. All the symbols are the same as panel (b). The sensitivity of the map is  $\sigma = 1.3$  mJy beam $^{-1}$ .

## 3.3. Jet Mass-loss Rate

we note that our fits ignore the likely high-velocity jet-structure (marked as “JET” in Figure 2(b), (d)) in the PV diagram, since the model of Lee et al. (2000) mainly describes the low-velocity winds. We did not incorporate with the jet-driven shell model, since no convex spur-like structures were observed in the PV diagram driven by the pulsating jet, as seen in the case of HH 212 (see Figure 13 by Lee et al. 2000).

Assuming optically thin CO emission, beam-averaged CO column densities ( $N_{\text{CO}}$ ) were estimated from the high-velocity channels of each lobe of each source. Here, the high-velocity channels are defined as  $|V - V_{\text{sys}}| > 65$  km s $^{-1}$  for G205S3 and  $> 45$  km s $^{-1}$  for G206W2 (Figure 1(a), (c)) up to a maximum velocity CO emission ( $V_{\text{max,CO}}$  in Table 1). The lower limits of the high velocities are adopted from the SiO emission, which

**Table 1**  
Outflow and Jet Parameters

Object	HOPS Id	C <sup>18</sup> O		SiO			CO			Corrected <sup>b</sup>	
		$V_{\text{sys}}$ (km s <sup>-1</sup> )	Lobe	$V_{\text{max,SiO}}^a$ (km s <sup>-1</sup> )	$N_{\text{SiO}}$ (10 <sup>15</sup> cm <sup>-2</sup> )	$V_{\text{max,CO}}$ (km s <sup>-1</sup> )	$i$ (deg)	$N_{\text{CO}}$ (10 <sup>17</sup> cm <sup>-2</sup> )	$(M)$ (10 <sup>-6</sup> M <sub>⊙</sub> yr <sup>-1</sup> )	$F_{\text{CO}}$ (10 <sup>-5</sup> M <sub>⊙</sub> km s <sup>-1</sup> yr <sup>-1</sup> )	
G205S3 (Class I)	315	9.9	Blue	106.7	0.37	109.5	40 ± 8	0.95	0.29	2.16	
			Red	120.1	0.22	96.3	40 ± 8	0.96	0.30	1.10	
G206W2 (Class 0)	399	8.8	Blue	81.8	1.30	76.4	10 ± 5	1.50	2.88	9.5	
			Red	103.0	1.21	76.2	10 ± 5	1.34	2.66	28.84	

**Notes.**

<sup>a</sup> The mean observed jet velocities for G205S3 and G206W2 are estimated as  $V_{j,\text{obs}} \sim 80$  and  $50$  km s<sup>-1</sup>, respectively.

<sup>b</sup> Corrected for inclination angles ( $i$ ).

include most of the jet emission. The mean intensity, integrated over velocity, is then obtained from the whole area encompassed by the jet emission. Assuming a specific excitation temperature of 150 K within the jet, the integrated intensity is converted into  $N_{\text{CO}}$ . The beam-averaged H<sub>2</sub> column density  $N_{\text{H}_2}$  is then derived assuming  $X_{\text{CO}}^{19} = N_{\text{CO}}/N_{\text{H}_2} = 4 \times 10^{-4}$  (Glassgold et al. 1991). The jet mass-loss rate ( $\dot{M}_j$ ) is obtained by assuming the jet as a uniform cylinder of gas flowing at constant density and speed along the jet axis over the transverse beam direction. Thus,  $\dot{M}_j$  within a single jet lobe is determined from

$$\dot{M}_j = \mu_{\text{H}_2} m_{\text{H}} \frac{N_{\text{CO}}}{X_{\text{CO}}} V_{j,\text{obs}} b_m, \quad (1)$$

where the mean molecular weight  $\mu_{\text{H}_2} = 2.8$  (e.g., Kauffmann et al. 2008),  $m_{\text{H}}$  is the mass of the hydrogen atom, and  $V_{j,\text{obs}}$  is the observed mean jet velocity (Section 3.1). The beam size ( $b_m$ ) transverse to the jet direction is assumed to be the jet width, since the jet is not resolved in the present spatial resolution.

The estimated values of  $N_{\text{CO}}$  and  $\dot{M}_j$  are listed in Table 1, with and without the inclination correction by using  $V_{j,\text{corr}}$  and  $V_{j,\text{obs}}$ , respectively. With these calculations, the total jet mass-loss rates are  $0.59 \times 10^{-6}$  and  $5.54 \times 10^{-6} M_{\odot} \text{ yr}^{-1}$  for G205S3 and G206W2, respectively. Such mass-loss rates are quite comparable to other protostars observed in the CALYPSO survey (Podio et al. 2021).

### 3.4. Outflow Force

Outflow momentum flux or force ( $F_{\text{CO}}$ ) is a vital ingredient to evaluate the outflow energetics of the protostars. From our limited field of view, we first estimated the outflow mass for each channel from the CO emission above  $3\sigma$  using the following equation (Yıldız et al. 2015):

$$M_k = \mu_{\text{H}_2} m_{\text{H}} A \frac{\sum_l N_{\text{CO},l}}{X_{\text{CO}}}. \quad (2)$$

Here,  $A$  is the surface area of one pixel and the sum is over all outflow pixels  $l$  on the  $k$ th channel. We assume a lower mean specific excitation temperature of  $T_{\text{ex}} = 50$  K and a less CO abundance ratio of  $X_{\text{CO}} \sim 10^{-4}$  for the outflow than that of the

<sup>19</sup> It might be as small as  $10^{-4}$ . In that case, the mass-loss rates would be increased by a factor of 4 (Hirano et al. 2010). The above estimation can thus be considered as the lower limit for the mass-loss rate.

jet. The momentum ( $P$ ) is calculated by multiplying each channel by the central velocity ( $V_k$ ) of the associated channel. The momentum is then integrated over all the channels from starting velocity ( $V_{\text{CO,min}}$ ) to maximum velocity ( $V_{\text{CO,max}}$ ) of CO emission over all pixels above  $3\sigma$  emission. Therefore, the  $F_{\text{CO}}$  can be expressed as (Yıldız et al. 2015)

$$F_{\text{CO}} = f_{\text{ia}} \frac{V_{\text{CO,max}} \sum_k M_k V_k}{R_{\text{CO}}}, \quad (3)$$

where  $f_{\text{ia}}$  is the inclination correction factor and  $R_{\text{CO}}$  is the length of the red and blueshifted outflow lobes. The measured values of  $F_{\text{CO}}$  for different lobes are listed in Table 1. The difference in red and blue lobe outflow occurs due to low signal-to-noise ratio, surrounding environment, and smaller field of view, which could not trace the whole outflow lobe in either direction and results in the apparently unequal extent of blue and redshifted lobes. Here, we note that changing  $T_{\text{ex}}$  by  $\pm 25$  K will change the estimated column densities by 10%–20%.

## 4. Discussion

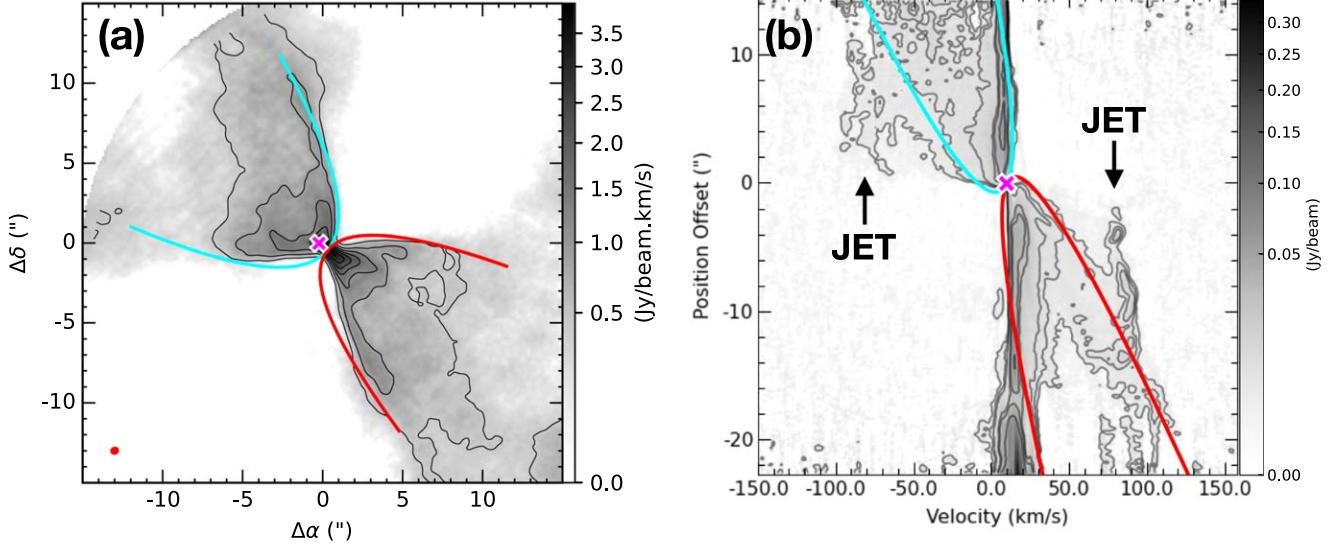
### 4.1. SiO Emission in Jet

At early protostellar phases, the outflow usually exhibits a higher mass-loss rate and produces higher density material than for later phases. Hence, SiO should be a better tracer of jets from earlier phase protostars, versus later phases (Glassgold et al. 1991; Shang et al. 2006, 2020; Cabrit et al. 2007). Therefore, the detection of SiO emission in jets is most likely indicating a younger phase of the protostars and a higher mass-loss rate. Such SiO emission is observed in several Class 0 protostars, e.g., B335 (Bjerkeli et al. 2019; Imai et al. 2019), HH 212 (Lee et al. 2017a, 2017b), L1157 (Tafalla et al. 2015; Podio et al. 2016), HH 211 (Jhan & Lee 2016; Lee et al. 2018), and IRAS 04166+2706 (Santiago-García et al. 2009; Tafalla et al. 2017).

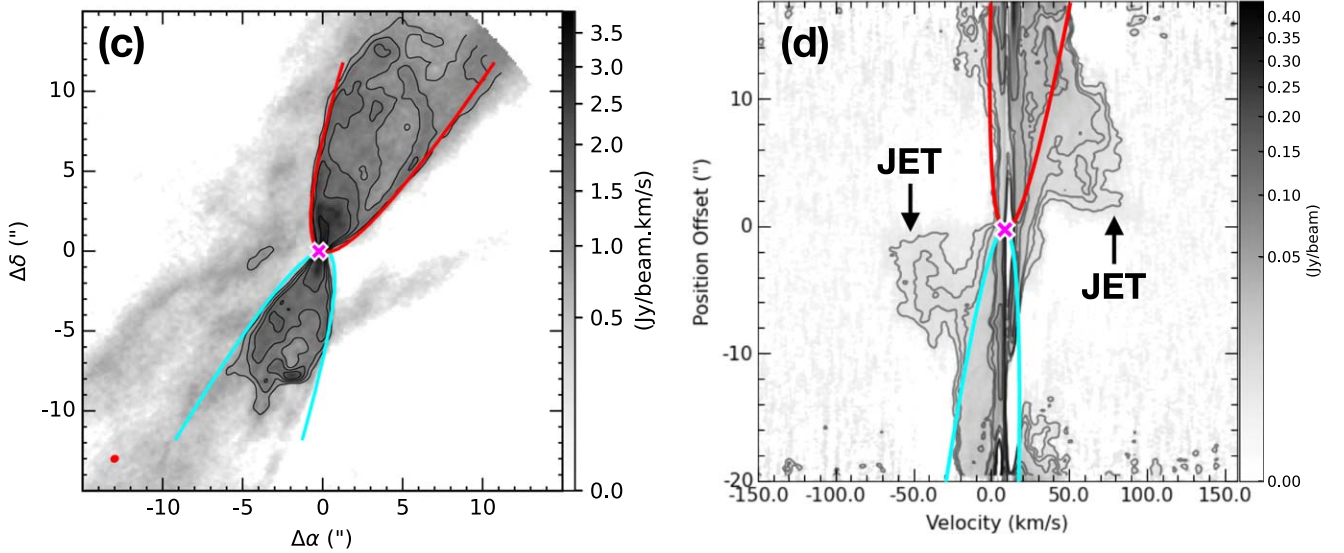
We observe SiO emission in the jet of a Class I source, G205S3. We estimated SiO column densities ( $N_{\text{SiO}}$ ) for G205S3 and G206W2 following the method described in Section 3.3, and the values are tabulated in Table 1. The SiO abundances ( $X_{\text{SiO}} = X_{\text{CO}} \times N_{\text{SiO}}/N_{\text{CO}}$ ) turn out to be  $1.25 \times 10^{-6}$  and  $3.5 \times 10^{-6}$  for G205S3 and G206W2, respectively. Similar types of SiO abundances were also observed in other protostellar jets in the literature (e.g., Podio et al. 2021). The denser jet of Class 0



## G205.46-14.56S3



## G206.93-16.61W2



**Figure 2.** (a) ALMA  $^{12}\text{CO}(2-1)$  map for G205S3. The black contours are at  $3n\sigma$ , where  $n = 1, 2, 3, \dots$  and  $\sigma = 0.16 \text{ Jy beam}^{-1} \text{ km s}^{-1}$ . The best-fit parabolas are shown for blueshifted (in blue) and redshifted (in red) outflow shell. The cross mark represents the source location. (b) PV diagram along the jet axis. The contours are at  $3 \times (1, 2, 3, 10, 16)\sigma$ , where  $\sigma = 0.0010 \text{ Jy beam}^{-1}$ . The parabolas in blueshifted (in blue) and redshifted (in red) components are best fits of the outflow shell for the corresponding estimated  $C$  values estimated in panel (a), with the best-fit  $i = 40^\circ$  (see text for details). The cross mark at  $(V_{\text{sys}}, 0)$  represent the source location. The high-velocity components are marked as “JET.” (c)  $^{12}\text{CO}(2-1)$  map for G206W3. All the symbols have the same meaning as panel (a), and the sensitivity is  $\sigma = 0.30 \text{ Jy beam}^{-1} \text{ km s}^{-1}$ . (d) PV diagram for G206W3 with the sensitivity of  $\sigma = 0.0011 \text{ Jy beam}^{-1}$ . All the symbols have the same meaning as those in panel (b). The best-fit inclination angle is  $i = 10^\circ$  for both lobes.

source G206W2 is possibly indicating a higher accretion phase than G205S3.

If we compare the integrated brightness temperatures of the SiO maps (Figure 1(a), (c)), G205S3 exhibits a fainter jet ( $\sim 200 \text{ K km s}^{-1}$ ) than G206W2 ( $\sim 1000 \text{ K km s}^{-1}$ ). For context, the Class 0 system, HH 212 exhibits an SiO integrated brightness temperature similar to that of G206W2 ( $\sim 1000 \text{ K km s}^{-1}$ ) (Lee et al. 2017a) and has a high mass-loss rate of  $\sim 1.1 \times 10^{-6} M_{\odot} \text{ yr}^{-1}$  (Lee et al. 2015). The fainter SiO jet indicates that G205S3 is arguably at the tail end of its *high-accretion* phase.

Previous high-resolution ALMA observations ( $\sim 8 \text{ au}$ ) of SiO jet near the base of HH 212 unveiled that the protostellar jets removed the residual angular momenta from the innermost part ( $\sim 0.05 \text{ au}$ ) region (Lee et al. 2017a). The bolometric luminosity ( $L_{\text{bol}} \sim 9 L_{\odot}$ ) of HH 212 suggests that SiO jet is possibly originating from the dust sublimated zone. From our SiO and CO emission, we estimated SiO-to-CO abundances ( $X[\text{SiO}/\text{CO}]$ ) are  $\sim 4 \times 10^{-3}$  and  $\sim 9 \times 10^{-3}$  for G205S3 and G206W2, respectively, which suggest that the jet is possibly launched from the dust-poor zones within the dust sublimation radius. Moreover, as Class 0 sources evolved to Class I, the  $X[\text{SiO}/\text{CO}]$  also declined

with decreasing mass-loss rate (Tabone et al. 2020). Lower SiO abundance in G205S3 than G206W2 could be related to evolutionary phases, although, a statistically more number of observations of Class 0 and Class I samples are required to constrain a systematic change in  $X[\text{SiO}/\text{CO}]$  with protostellar evolution. Here, we note that the SiO line could be optically thick even in the high-velocity jet (e.g., Podio et al. 2021). Since CO is likely optically thin in the jet, the SiO-to-CO abundance ratio derived here could constitute a lower limit to the true SiO-to-CO abundance ratio.

More specifically, comparing the mass-loss rate and  $X[\text{SiO}/\text{CO}]$  with the astrochemical models of Tabone et al. (2020; see their Figure 12), the SiO-rich jet of G206W2 is expected to be launched from the dust sublimation zones. The jet of G205S3 could have been launched even from the dust-poor zones (dust mass fraction  $\sim 10^{-3}$ ), which could be the outer boundary of dust sublimation zones. The bolometric luminosities of both G205S3 and G206W2 suggest that their dust sublimation radii are less than 0.1 au (Millan-Gabet et al. 2007). Silicon is possibly released into the gas phase near the base of the jet and can synthesize SiO molecules (Glassgold et al. 1991). For low-luminosity objects,  $\text{Si}^+$  recombination and SiO formation occur faster than the photodissociation by the relatively weak ultraviolet radiation from the central protostar, yielding abundant SiO.

To summarize, we surprisingly detected SiO emission in the jet of evolved Class I source G205S3, as usually observed in Class 0 sources (e.g., G206W2, HH 212) in this study as well as in the literature. To validate the true evolutionary phase of G205S3, we investigate the aspects of possible misclassification of G205S3.

## 4.2. Evolutionary Status

### 4.2.1. Inclination Effect

The spectral classifications through  $T_{\text{bol}}$  and  $\alpha_{\text{IR}}$  of protostars are based on the observed fluxes of the component central source, disk, and envelope, obtained by telescopes with different spatial resolutions. The system's inclination angle to the line of sight, however, constitutes a major uncertainty to the interpretation of the observed fluxes, given the asymmetries inherent in the circumstellar environment (Evans et al. 2009; Furlan et al. 2016). For example, the face-on view of a flattened envelope-disk (or pole-on outflow) yields relatively high infrared fluxes due to less extinction along the line of sight compared with an edge-on view (pole-off outflow) of the same system. Thus, as a result, a Class 0 source may appear to be Class I. Disentangling observed fluxes and inclination angles can be difficult. Fortunately, however, Furlan et al. (2016) modeled the spectral energy distributions (SEDs) of protostars at different inclination angles. Indeed, their models suggest an inclination angle of  $50^\circ$  for both sources. Although the SED-derived inclination angle of G205S3 is close to that measured from the outflow morphology ( $\sim 40^\circ$ ; Table 1), that of G206W2 is more dissimilar to the inclination angle suggested by its outflow ( $\sim 10^\circ$ ).

We applied the inclination effect when determining mass-loss rates in Table 1. Nevertheless, the mass-loss rate of G205S3 remains at the lower end of what is expected for Class 0 systems. At present, it is not clear how much the inclination affects the spectral classification of G205S3. It is also difficult to predict how significantly the inclination of  $40^\circ$ –

$60^\circ$  might expose the central source to the observer, given that the object is still not close to face-on. Therefore, we probe other evidence to validate the evolutionary status of the sources, such as (i) outflow energetics, (ii)  $\text{C}^{18}\text{O}$  emission and surrounding material, and (iii) luminosity versus millimeter flux, in the next sections.

### 4.2.2. Outflow Energetics

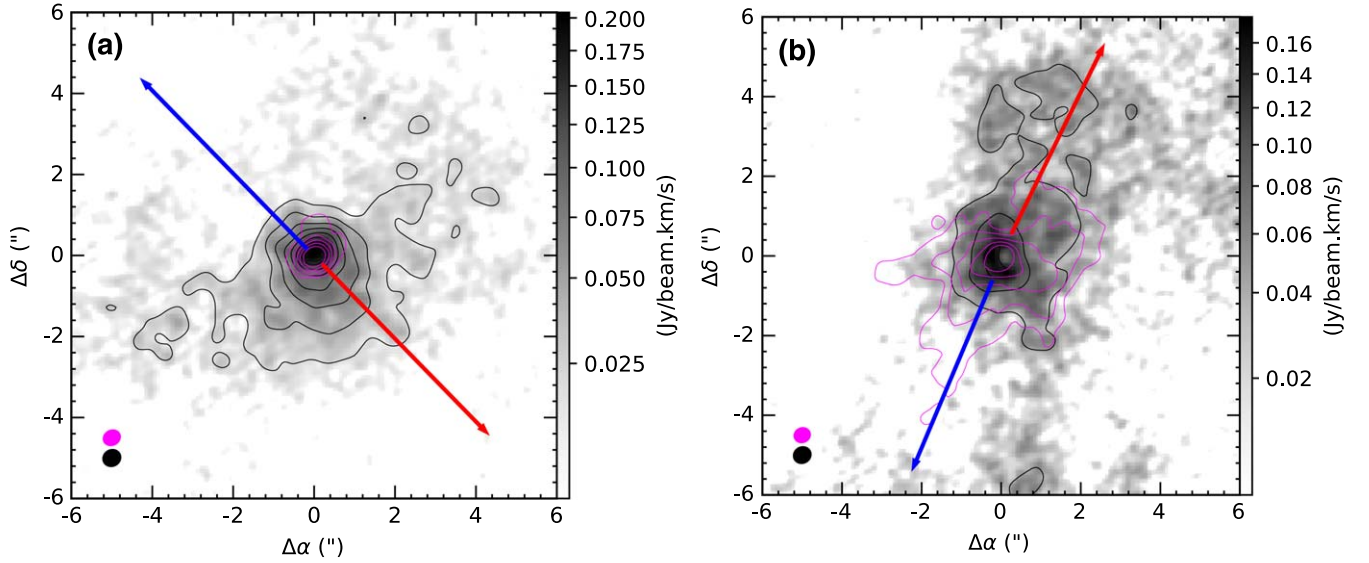
Previous observations revealed that a Class I source usually exhibits smaller  $F_{\text{CO}}$  than Class 0 with similar  $L_{\text{bol}}$  (Bontemps et al. 1996; Hatchell et al. 2007; Curtis et al. 2010; Yıldız et al. 2015), which suggest that the Class 0 sources are more energetic than the Class I counterpart. Assuming a CO abundance ratio of  $1.2 \times 10^{-4}$ , Yıldız et al. (2015) obtained the typical values of  $F_{\text{CO}} \sim 2.8 \times 10^{-5} M_\odot \text{ km s}^{-1} \text{ yr}^{-1}$  for Class I sources, and  $\sim 6.9 \times 10^{-4} M_\odot \text{ km s}^{-1} \text{ yr}^{-1}$  for Class 0 sources. We estimated a total of  $F_{\text{CO}} \sim 3.26 \times 10^{-5} M_\odot \text{ km s}^{-1} \text{ yr}^{-1}$  for G205S3 and  $\sim 3.834 \times 10^{-4} M_\odot \text{ km s}^{-1} \text{ yr}^{-1}$  for G206W2 (Table 1). The smaller  $F_{\text{CO}}$  of G205S3 make it more similar to a Class I source, whereas the relatively high value  $F_{\text{CO}}$  indicate that G206W2 is probably a Class 0 source.

### 4.2.3. $\text{C}^{18}\text{O}$ Emission and Surrounding Material

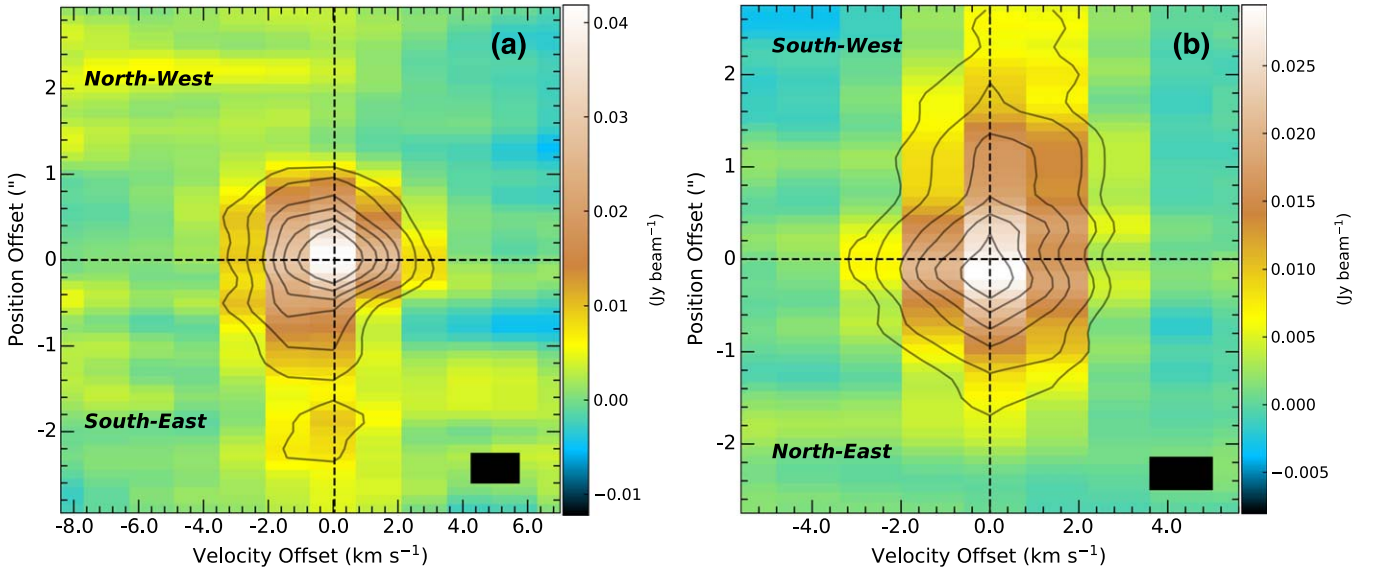
The bolometric temperature ( $\sim 180$  K) and near-infrared spectral index ( $\alpha_{\text{IR}} \sim 0.417$ ) suggest that G205S3 is a Class I source (Furlan et al. 2016; Dutta et al. 2020). In addition, if we compare Figures 3(a) and (b), G205S3 displays relatively compact  $\text{C}^{18}\text{O}$  and 1.33 mm continuum emission compared with G206W2. The disk-envelope mass of G205S3,  $\sim 0.167 \pm 0.072 M_\odot$ , is a few times smaller than G206W2,  $\sim 0.771 \pm 0.333 M_\odot$ , at the same beam resolution,  $\sim 140$  au (Dutta et al. 2020). Such compact emission in G205S3 is consistent with a smaller envelope surrounding the protostar, with the emission most likely emanating from an evolved disk, consistent with a Class I object. For G206W2, the envelope dominates the observed emission, consistent with a very early, Class 0, stage of protostellar evolution. It is to be noted that the compactness of a source based on continuum or line images (e.g.,  $\text{C}^{18}\text{O}$ ) largely depends on the sensitivity of the maps.

To extract the size of compact components, we explore the continuum visibility amplitudes (Jy) as a function of  $uv$  distance ( $k\lambda$ ). Following Lee et al. (2008), the  $uv$  visibilities were fitted with two Gaussian components. The compact component of G205S3 has a deconvolved size of  $\sim 0''.20$  and flux  $\sim 30$  mJy. The extended component has a deconvolved size of  $\sim 2''.28$  and flux  $\sim 47$  mJy. Similarly, G206W2 has a compact component of size  $\sim 0''.60$  (flux  $\sim 100$  mJy) and extended component  $\sim 2''.55$  (flux  $\sim 320$  mJy). These sizes of compact component are consistent with 1.3 mm continuum, as estimated by Dutta et al. (2020). From the  $uv$  domain, These results also suggest that G205S3 possesses a relatively compact core, surrounded by a relatively smaller envelope.

Larger-scale James Clerk Maxwell Telescope (JCMT) observations (beam size  $\sim 5600$  au) also reveal a relatively compact core surrounding the G205S3 (size  $\sim 0.04$  pc; mass  $\sim 0.86 \pm 0.16 M_\odot$ ) compared with G206W2 (size  $\sim 0.06$  pc; mass  $\sim 3.38 \pm 0.15 M_\odot$ ) (Yi et al. 2018). Here, we remark that the significant amount of gas in the core should be resolved out by the interferometric ALMA observations. Thus, the interpretation of the compact emission distribution may depend



**Figure 3.** ALMA  $C^{18}O$  maps for G205S3 (a) and G206W2 (b). The black  $C^{18}O$  contours are at  $3n\sigma$ , where  $n = 2, 3, 4, \dots$  and  $\sigma = 0.007$  and  $0.015 \text{ Jy beam}^{-1} \text{ km s}^{-1}$  in panels (a) and (b), respectively. The magenta contours are the 1.3 mm continuum at  $\sum_{n=1,2,3,\dots} 3 \times 2^n \sigma$ , where  $\sigma = 8 \times 10^{-5} \text{ Jy beam}^{-1}$  (panel (a)) and  $15 \times 10^{-5} \text{ Jy beam}^{-1}$  (panel (b)). The synthesized beams are shown in black ( $C^{18}O$ ) and magenta (continuum) in the lower left. The red and blue arrows indicate the redshifted and blueshifted jet axis.



**Figure 4.**  $C^{18}O$  PV diagram along perpendicular to jet axis for (a) G205S3 and (b) G206W2. The source location is at the center of the cross mark. The beam size and velocity resolution are shown with black rectangle at lower right of each panel.

somewhat on the spatial resolution of the envelope observations.

The  $C^{18}O$  PV diagram is shown in Figure 4. Similar to Figure 3, G205S3 appears more compact than G206W2 in PV space. The  $C^{18}O$  emission is most likely originating from the envelope part of both the sources. No Keplerian rotation profiles are observed clearly on both sources. Higher spatial and velocity resolution data could efficiently determine the Keplerian rotation from the inner part and possibly allow to measure protostellar masses (e.g., Lee et al. 2014), and hence could constrain the evolutionary phases of the stellar cores.

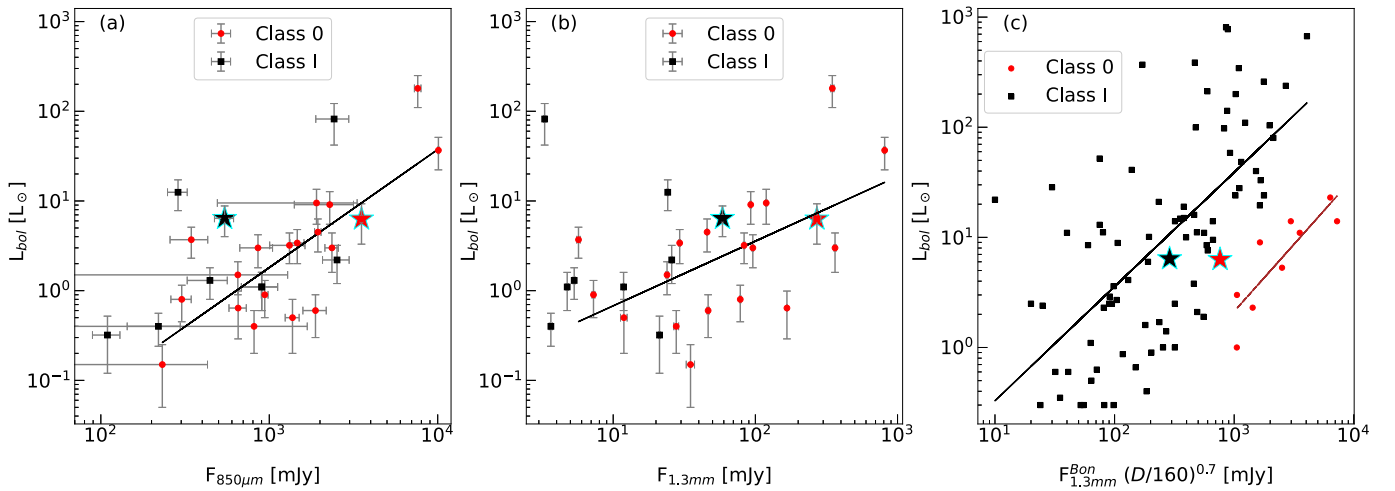
#### 4.2.4. Luminosity and Flux Correlation

The (sub)millimeter and far-IR fluxes contribute more to  $L_{\text{bol}}$  for the Class 0 than that of Class I sources since these fluxes

mostly originate from the envelope and Class 0 should have larger surrounding material. In Figure 5, luminosities of the Class 0 and Class I sources are shown as a function of JCMT  $870 \mu\text{m}$  (panel (a)) and ALMA 1.3 mm (panel (b)) fluxes for the non-multiple<sup>20</sup> ALMASOP sources (see Dutta et al. 2020). A linear fit only for the Class 0 sources are also shown in both panels. No obvious correlation was found between the Class 0 and Class I sources. One interesting fact is that most of the Class I sources,  $\sim 75\%$  for  $870 \mu\text{m}$  (panel (a)) and  $\sim 90\%$  for 1.3 mm (panel (b)), are located above the locus of Class 0 sources (black fitted line). Our studied targets, G205S3 (Class I:  $L_{\text{bol}} = 6.4 \pm 2.4 L_{\odot}$ ) and G206W2 (Class 0:  $L_{\text{bol}} = 6.3 \pm 3.0 L_{\odot}$ ) have similar type of

<sup>20</sup> Luminosity of multiple systems is contributed from the different protostellar components within the common envelope. To reduce the uncertainty in the correlation, we removed the known multiple sources from this analysis.





**Figure 5.** Flux vs. bolometric luminosity for Class 0 (red circle) and Class I (black square) for the ALMASOP sources (panels (a) and (b)) from Dutta et al. (2020). The solid lines in panels (a) and (b) indicate the best-fit correlation for the Class 0 sources only. The star marks indicate Class 0 (G206W2 in red) and Class I (G205S3 in black) sources, studied in this paper. Panel (a) utilizes JCMT 850  $\mu m$  fluxes and panel (b) utilizes the ALMA 1.3 mm fluxes. In panel (c), G205S3 and G206W2 are compared with the Class 0 and Class I sample of Saraceno et al. (1996). The solid black line is the best fit for the Class I sources and the brown line is the best fit for Class 0 sources.

luminosities. However, if we see their location in Figure 5, G205S3 (black star mark) exhibit lower fluxes than G206W2 (red star mark) in both 870  $\mu m$  (panel (a)) and 1.3 mm emission (panel (b)). Here, we note that the use of single-dish data (JCMT) would reduce the contamination by a possible massive disk in Class I sources than interferometer (ALMA), and the low-resolution JCMT data could include significant emission from the larger scale cloud emission beyond the envelope and presence of possible multiple sources. Both could potentially affect the interpretation of flux-luminosity correlation.

A similar type of correlation was also studied for 1.3 mm fluxes of Class 0 and Class I sources in Reipurth et al. (1993) and Saraceno et al. (1996). We adopted the single-dish observations of Class 0 and Class I sample from Saraceno et al. (1996) in Figure 5(c). We scale down 870  $\mu m$  JCMT single-dish observations of G205S3 (black star mark) and G206W2 (red star mark) from Dutta et al. (2020) to 1.3 mm fluxes with spectral index 3.0 and 160 pc distance with a distance correlation from Saraceno et al. (1996). With their limited number of Class 0 sample, G205S3 is quite convincingly located in Class I cluster and G206W2 is located near the Class 0 cluster. Such correlations are quite obvious and could be utilized to distinguish between different spectral classes. More robust single-dish observations at 1.3 mm of a larger sample of Class I and Class 0 sources are needed to constrain the correlation.

#### 4.3. Jets Knots and Accretion Variability

Variable accretion may be due to a circumbinary disk around a close binary, potentially affecting the final mass budget of the binary and planet formation (Günther & Kley 2002; Shi et al. 2012). Periodic variations due to pulsed accretion have been observed in T Tauri binary systems (e.g., DQ Tau: Mathieu et al. 1997); (UZ Tau E: Jensen et al. 2007). Another Class I, possibly binary, system LRL 54361 has pulsed accretion with a high-accretion rate of  $3 \times 10^{-6} M_{\odot} \text{yr}^{-1}$  (Muzerolle et al. 2013).

The JCMT Transient Survey (Herczeg et al. 2017) has been monitoring Class 0 and I protostars in submillimeter continuum

for over 4 yr, with monthly cadence (Johnstone et al. 2018; Lee et al. 2021). G205S3 is a JCMT-monitored variable, with an extrapolated episode timescale  $\sim 8$  yr, and an implied 10% mass accretion rate variability (Lee et al. 2021). Similar variability properties are found in the mid-infrared (mid-IR) (Park et al. 2021). G206W2 is not included in the JCMT sample and it is too bright for inclusion in the mid-IR analysis by Park et al. (2021). Extracting the light curve from the NEOWISE catalog (W. Park 2021, private communication) reveals a long-timescale secular change in brightness.

The G205S3 SiO jet knots imply ejection episodes  $54^{+30}_{-10}$  yr apart ( $\Delta r_{\text{corr}}/V_{j,\text{corr}}$ ; Section 3.1), longer than the extrapolated accretion event uncovered by the JCMT. A statistical ensemble analysis of the JCMT protostars suggests that these burst events typically occur every  $\sim 50$  yr, consistent with the G205S3 knot separation. Repetitive ejection may be related to episodic accretion of dense clumps created by instabilities within a massive disk or magnetorotational instabilities (Machida et al. 2011; Bae et al. 2014; Vorobyov & Basu 2015). Alternatively, embedded planetesimals or a circumbinary disk due to an unresolved binary might create periodic accretion signatures (Bonnell & Bastien 1992; Muñoz & Lai 2016). However, observationally no binary has been detected in the G205S3 system so far. G206W2 exhibits ejections with a  $17^{+30}_{-10}$  yr timescale, more closely matching the extrapolated mid-IR light curve. Further high spatial resolution outflow studies and continued mid-IR through submillimeter monitoring are required to better diagnose the underlying accretion-ejection scenarios.

## 5. Conclusions

We detect SiO jet emission and a moderately high mass-loss rate of  $\sim 0.59 \times 10^{-6} M_{\odot} \text{yr}^{-1}$  for the isolated Class I source, G205S3. These outflow features are more typically seen in younger, Class 0 sources like the representative source G206W2 ( $M_j \sim 5.54 \times 10^{-6} M_{\odot} \text{yr}^{-1}$ ). We estimated a high inclination ( $i \sim 40^\circ$ ) of G205S3. Perhaps G205S3 has been misidentified as Class I from the SED of observed fluxes due to its high inclination. However, the compact 1.3 mm continuum,  $C^{18}O$  emission, location in the bolometric








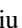


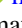



luminosity and submillimeter fluxes diagram, lower SiO-to-CO abundances ( $\sim 4 \times 10^{-3}$ ) in the jet are consistent with a Class I system. The SiO-to-CO abundances, mass-loss rate, and bolometric luminosity indicate that the jets from both the sources, G205S3 and G206W2, are possibly launched from the innermost dust-poor zones. The measured values of outflow forces,  $F_{\text{CO}} \sim 3.26 \times 10^{-5} M_{\odot} \text{ km s}^{-1} \text{ yr}^{-1}$  for G205S3 and  $\sim 3.834 \times 10^{-4} M_{\odot} \text{ km s}^{-1} \text{ yr}^{-1}$  for G206W2 infer that G205S3 could be a Class I, whereas G206W2 is possibly a Class 0 source. The episodic ejection could be due to the presence of an unknown binary, a planetary companion, or dense clumps in a circumbinary disk, which also could trigger such high accretion. Alternatively, some special environmental conditions or rare orbital parameters may be in play that favors the high-accretion rate. Further high-resolution near-IR and ALMA observations are needed.














We thank the anonymous referee for the constructive comments. This paper makes use of the following ALMA data: ADS/JAO.ALMA#2018.1.00302.S. ALMA is a partnership of ESO (representing its member states), NSF (USA) and NINS (Japan), together with NRC (Canada), NSC and ASIAA (Taiwan), and KASI (Republic of Korea), in cooperation with the Republic of Chile. The Joint ALMA Observatory is operated by ESO, AUI/NRAO and NAOJ. S.D. and C.-F.L. acknowledge grants from the Ministry of Science and Technology of Taiwan (MoST 107-2119-M-001-040-MY3) and the Academia Sinica (Investigator Award AS-IA-108-M01). C.W.L. is supported by the Basic Science Research Program through the National Research Foundation of Korea (NRF) funded by the Ministry of Education, Science and Technology (NRF-2019R1A2C1010851). D.J. is supported by the National Research Council of Canada and by a Natural Sciences and Engineering Research Council of Canada (NSERC) Discovery Grant. T.L. acknowledges the support from the National Natural Science Foundation of China (NSFC) through grants No. 12073061 and No. 12122307, the international partnership program of Chinese Academy of Sciences through grant No. 114231KYSB20200009, and Shanghai Pujiang Program 20PJ1415500. P.S. was partially supported by a Grant-in-Aid for Scientific Research (KAKENHI No. 18H01259) of the Japan Society for the Promotion of Science (JSPS). L.B. acknowledges support from ANID project Basal AFB-170002.

*Facility:* ALMA.

*Software:* Astropy (Astropy Collaboration et al. 2013), APLpy (Robitaille & Bressert 2012), Matplotlib (Hunter 2007), CASA (McMullin et al. 2007).

### ORCID iDs

Somnath Dutta  <https://orcid.org/0000-0002-2338-4583>  
 Chin-Fei Lee  <https://orcid.org/0000-0002-3024-5864>  
 Doug Johnstone  <https://orcid.org/0000-0002-6773-459X>  
 Tie Liu  <https://orcid.org/0000-0002-5286-2564>  
 Naomi Hirano  <https://orcid.org/0000-0001-9304-7884>  
 Sheng-Yuan Liu  <https://orcid.org/0000-0003-4603-7119>  
 Jeong-Eun Lee  <https://orcid.org/0000-0003-3119-2087>  
 Hsien Shang  <https://orcid.org/0000-0001-8385-9838>  
 Ken'ichi Tatematsu  <https://orcid.org/0000-0002-8149-8546>  
 Kee-Tae Kim  <https://orcid.org/0000-0003-2412-7092>  
 Dipen Sahu  <https://orcid.org/0000-0002-4393-3463>  
 Patricio Sanhueza  <https://orcid.org/0000-0002-7125-7685>

James Di Francesco  <https://orcid.org/0000-0002-9289-2450>  
 Kai-Syun Jhan  <https://orcid.org/0000-0003-2069-1403>  
 Chang Won Lee  <https://orcid.org/0000-0002-3179-6334>  
 Woojin Kwon  <https://orcid.org/0000-0003-4022-4132>  
 Shanghuo Li  <https://orcid.org/0000-0003-1275-5251>  
 Leonardo Bronfman  <https://orcid.org/0000-0002-9574-8454>  
 Hong-li Liu  <https://orcid.org/0000-0003-3343-9645>  
 Alessio Traficante  <https://orcid.org/0000-0003-1665-6402>  
 Yi-Jehng Kuan  <https://orcid.org/0000-0002-4336-0730>  
 Shih-Ying Hsu  <https://orcid.org/0000-0002-1369-1563>  
 Chun-Fan Liu  <https://orcid.org/0000-0002-1624-6545>  
 David Eden  <https://orcid.org/0000-0002-5881-3229>  
 Archana Soam  <https://orcid.org/0000-0002-6386-2906>

### References

- Astropy Collaboration, Robitaille, T. P., Tollerud, E. J., et al. 2013, *A&A*, **558**, A33
- Bachiller, R., Gueth, F., Guilloteau, S., Tafalla, M., & Dutrey, A. 2000, *A&A*, **362**, L33
- Bae, J., Hartmann, L., Zhu, Z., & Nelson, R. P. 2014, *ApJ*, **795**, 61
- Bally, J. 2016, *ARA&A*, **54**, 491
- Bjerkeli, P., Ramsey, J. P., Harsono, D., et al. 2019, *A&A*, **631**, A64
- Bonnell, I., & Bastien, P. 1992, *ApJL*, **401**, L31
- Bontemps, S., Andre, P., Terebey, S., & Cabrit, S. 1996, *A&A*, **311**, 858
- Cabrit, S., Codella, C., Gueth, F., et al. 2007, *A&A*, **468**, L29
- Chen, H., Myers, P. C., Ladd, E. F., & Wood, D. O. S. 1995, *ApJ*, **445**, 377
- Curtis, E. I., Richer, J. S., Swift, J. J., & Williams, J. P. 2010, *MNRAS*, **408**, 1516
- Dutta, S., Lee, C.-F., Liu, T., et al. 2020, *ApJS*, **251**, 20
- Ellerbroek, L. E., Podio, L., Kaper, L., et al. 2013, *A&A*, **551**, A5
- Evans, N. J. I., Dunham, M. M., Jørgensen, J. K., et al. 2009, *ApJS*, **181**, 321
- Furlan, E., Fischer, W. J., Ali, B., et al. 2016, *ApJS*, **224**, 5
- Gibb, A. G., Richer, J. S., Chandler, C. J., & Davis, C. J. 2004, *ApJ*, **603**, 198
- Glassgold, A. E., Mamon, G. A., & Huggins, P. J. 1991, *ApJ*, **373**, 254
- Günther, R., & Kley, W. 2002, *A&A*, **387**, 550
- Hatchell, J., Fuller, G. A., & Richer, J. S. 2007, *A&A*, **472**, 187
- Herczeg, G. J., Johnstone, D., Mairs, S., et al. 2017, *ApJ*, **849**, 43
- Hirano, N., Ho, P. P. T., Liu, S.-Y., et al. 2010, *ApJ*, **717**, 58
- Hunter, J. D. 2007, *CSE*, **9**, 90
- Imai, M., Oya, Y., Sakai, N., et al. 2019, *ApJL*, **873**, L21
- Jensen, E. L. N., Dhital, S., Stassun, K. G., et al. 2007, *AJ*, **134**, 241
- Jhan, K.-S., & Lee, C.-F. 2016, *ApJ*, **816**, 32
- Johnstone, D., Herczeg, G. J., Mairs, S., et al. 2018, *ApJ*, **854**, 31
- Kauffmann, J., Bertoldi, F., Bourke, T. L., Evans, N. J. I., & Lee, C. W. 2008, *A&A*, **487**, 993
- Lee, C.-F. 2020, *A&ARv*, **28**, 1
- Lee, C.-F., Hirano, N., Zhang, Q., et al. 2014, *ApJ*, **786**, 114
- Lee, C.-F., Hirano, N., Zhang, Q., et al. 2015, *ApJ*, **805**, 186
- Lee, C.-F., Ho, P. T. P., Bourke, T. L., et al. 2008, *ApJ*, **685**, 1026
- Lee, C.-F., Ho, P. T. P., Li, Z.-Y., et al. 2017a, *NatAs*, **1**, 0152
- Lee, C.-F., Li, Z.-Y., Hirano, N., et al. 2018, *ApJ*, **863**, 94
- Lee, C.-F., Li, Z.-Y., Ho, P. T. P., et al. 2017b, *SciA*, **3**, e1602935
- Lee, C.-F., Mundy, L. G., Reipurth, B., Ostriker, E. C., & Stone, J. M. 2000, *ApJ*, **542**, 925
- Lee, Y.-H., Johnstone, D., Lee, J.-E., et al. 2021, *ApJ*, **920**, 119
- Lefèvre, C., Cabrit, S., Maury, A. J., et al. 2017, *A&A*, **604**, L1
- Machida, M. N., Inutsuka, S.-i., & Matsumoto, T. 2011, *ApJ*, **729**, 42
- Mathieu, R. D., Stassun, K., Basri, G., et al. 1997, *AJ*, **113**, 1841
- McMullin, J. P., Waters, B., Schiebel, D., Young, W., & Golap, K. 2007, in ASP Conf. Ser. 376, *CASA Architecture and Applications*, ed. R. A. Shaw, F. Hill, & D. J. Bell (San Francisco, CA: ASP), 127
- Millan-Gabet, R., Malbet, F., Akeson, R., et al. 2007, in *Protostars and Planets V*, ed. B. Reipurth, D. Jewitt, & K. Keil (Tucson, AZ: Univ. Arizona Press), 539
- Moraghan, A., Lee, C.-F., Huang, P.-S., & Vaidya, B. 2016, *MNRAS*, **460**, 1829
- Muñoz, D. J., & Lai, D. 2016, *ApJ*, **827**, 43
- Muzerolle, J., Furlan, E., Flaherty, K., Balog, Z., & Gutermuth, R. 2013, *Natur*, **493**, 378
- Park, W., Lee, J.-E., Contreras Peña, C., et al. 2021, *ApJ*, **920**, 132
- Podio, L., Codella, C., Gueth, F., et al. 2015, *A&A*, **581**, A85

- Podio, L., Codella, C., Gueth, F., et al. 2016, [A&A](#), **593**, L4
- Podio, L., Tabone, B., Codella, C., et al. 2021, [A&A](#), **648**, A45
- Reipurth, B., Chini, R., Krugel, E., Kreysa, E., & Sievers, A. 1993, [A&A](#), **273**, 221
- Robitaille, T., & Bressert, E. 2012, APLpy: Astronomical Plotting Library in Python, Astrophysics Source Code Library, ascl:1208.017
- Santiago-García, J., Tafalla, M., Johnstone, D., & Bachiller, R. 2009, [A&A](#), **495**, 169
- Saraceno, P., Andre, P., Ceccarelli, C., Griffin, M., & Molinari, S. 1996, [A&A](#), **309**, 827
- Shang, H., Allen, A., Li, Z.-Y., et al. 2006, [ApJ](#), **649**, 845
- Shang, H., Krasnopolsky, R., Liu, C.-F., & Wang, L.-Y. 2020, [ApJ](#), **905**, 116
- Shi, J.-M., Krolik, J. H., Lubow, S. H., & Hawley, J. F. 2012, [ApJ](#), **749**, 118
- Tabone, B., Godard, B., Pineau des Forêts, G., Cabrit, S., & van Dishoeck, E. F. 2020, [A&A](#), **636**, A60
- Tafalla, M., Bachiller, R., Lefloch, B., et al. 2015, [A&A](#), **573**, L2
- Tafalla, M., Su, Y. N., Shang, H., et al. 2017, [A&A](#), **597**, A119
- Vorobyov, E. I., & Basu, S. 2015, [ApJ](#), **805**, 115
- Wang, L.-Y., Shang, H., & Chiang, T.-Y. 2019, [ApJ](#), **874**, 31
- Yi, H.-W., Lee, J.-E., Liu, T., et al. 2018, [ApJS](#), **236**, 51
- Yıldız, U. A., Kristensen, L. E., van Dishoeck, E. F., et al. 2015, [A&A](#), **576**, A109